ACS Sustainable Chemistry & Engineering

Research Article

pubs.acs.org/journal/ascecg

Photovoltaic Property of Anatase TiO_2 3-D Mesoflowers

T. G. Deepak, Devika Subash, G. S. Anjusree, K. R. Narendra Pai, Shantikumar V. Nair, and A. Sreekumaran Nair*

Amrita Centre for Nanosciences and Molecular Medicine, Amrita Institute of Medical Sciences, Amrita Vishwa Vidyapeetham, AIMS PO, Ponekkara, Kochi 682041, Kerala, India

ABSTRACT: We have synthesized 3-D flower-like mesostructured TiO_2 from one-dimensional electrospun TiO_2−SiO_2 nanocomposites through a modified titanate route for dye-sensitized solar cell (DSC) application. The TiO_2 3-D mesoflowers with commendable internal surface area, crystallinity, and a good light scattering property satisfy the prerequisites of a DSC photoanode material. The starting TiO_2−SiO_2 composite, intermediate titanate, and final 3-D mesoflowered TiO_2 were characterized by spectroscopy, microscopy, and surface area measurements. A DSC employing 3-D mesoflowered TiO_2 as the photoanode showed a power conversion efficiency of 8.3% which was 23% higher than that of commercial P-25 (6.37%).

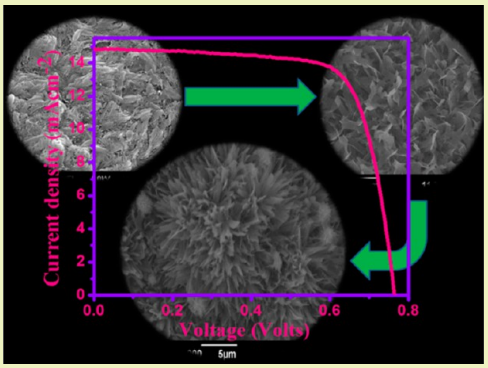

KEYWORDS: *Dye-sensitized solar cell, TiO_2, TiO_2−SiO_2 composite, Light scattering, Electrochemical impedance spectroscopy*

INTRODUCTION

TiO_2 is a material for multifaceted applications in areas such as dye-sensitized solar cells (DSCs), storage devices, photonic crystals, self-cleaning coatings, environmental remediation, water purification, etc.[1−9] DSCs, first presented by O'Regan and Grätzel in 1991, marked a paradigm shift in the area of renewable energy research.[10] DSC is still considered as one of the options for harnessing solar energy as it employs environmentally benign and relatively cheap raw materials for its making in addition to fabrication feasibilities under nonvacuum conditions. TiO_2 forms the backbone of DSCs as it performs the dual functions of supporting the sensitizers (the dyes) and charge transport. Sensitizer loading on TiO_2 is directly related to its density, surface area, and phase purity, and smooth charge transport is a measure of its crystallinity. Thus, fabrication of dense, crystalline, and high surface area TiO_2 is essential to have efficient DSC devices.

Many researchers have investigated the usefulness of electrospun TiO_2 nanofibers for DSCs but ended up with a lower efficiency in the range of 4−5% in lab-scale research.[11−15] Although nanofibers have beneficial aspects such as semidirected electron transport and the presence of straight pores in one-dimensional architecture that facilitates effective electrode wetting by electrolyte species, their internal surface area is very low, which prevents good dye chemisorption.[14−16] Thus, to promote the use of electrospun TiO_2 in DSCs and photocatalysis, it is necessary to find ways to improve their surface areas through chemical means. We have found that the titanate route, which is the chemical conversion of TiO_2 into $Na_2Ti_3O_7$ (sodium titanate) by concentrated NaOH/KOH and subsequent conversion of the $Na_2Ti_3O_7$ back into TiO_2, leads to improved surface areas.[17−19] The route has been demonstrated in the case of P-25 TiO_2 (spherical TiO_2 particles of ∼25 nm average diameter), which with titanate chemistry leads to the formation of TiO_2 nanorods/nanowires.[20,21] We have adopted titanate chemistry in electrospun TiO_2−SiO_2 composite nanofibers.[18,19] The rationale for incorporating SiO_2 along with TiO_2 in the nanofibers is that SiO_2 is an acidic oxide that can be completely etched by NaOH (during the titanate chemistry), and we demonstrated previously that etching of one of the components from a composite metal oxide system will lead to high surface area for the unetched metal oxide in addition to structural anisotropy.[22,23] When we adopted the titanate route on the electrospun TiO_2−SiO_2 composite fibers, the result was unexpected 3-D mesoflowers with high surface areas of 166 m^2/g and good crystallinity.[17] The usefulness of the material was tested only for photocatalysis, and the present manuscript investigates its utility in DSCs.

The initial TiO_2−SiO_2 composite fibers, intermediate $Na_2Ti_3O_7$, and final TiO_2 mesoflowers were characterized by spectroscopy, microscopy, powder XRD, and surface area measurements. The 3-D mesoflowers were employed in a DSC, which showed a power conversion efficiency of 8.3% (for a square-shaped cell of 0.20 cm^2 area and 14 μm thickness) in comparison to 6.37% for the commercially available P-25 (both had similar electrode parameters). The IPCE measurements of the devices was ∼80% for the 3-D mesoflowers vs ∼66% for P-25. The DSCs were additionally characterized by dye loading and electrochemical impedance measurements. It must be noted that an efficiency of 8.3% from the mesoflowers is an impressive value

Received: August 18, 2014
Published: October 21, 2014

   dx.doi.org/10.1021/sc500642c | *ACS Sustainable Chem. Eng.* 2014, 2, 2772−2780

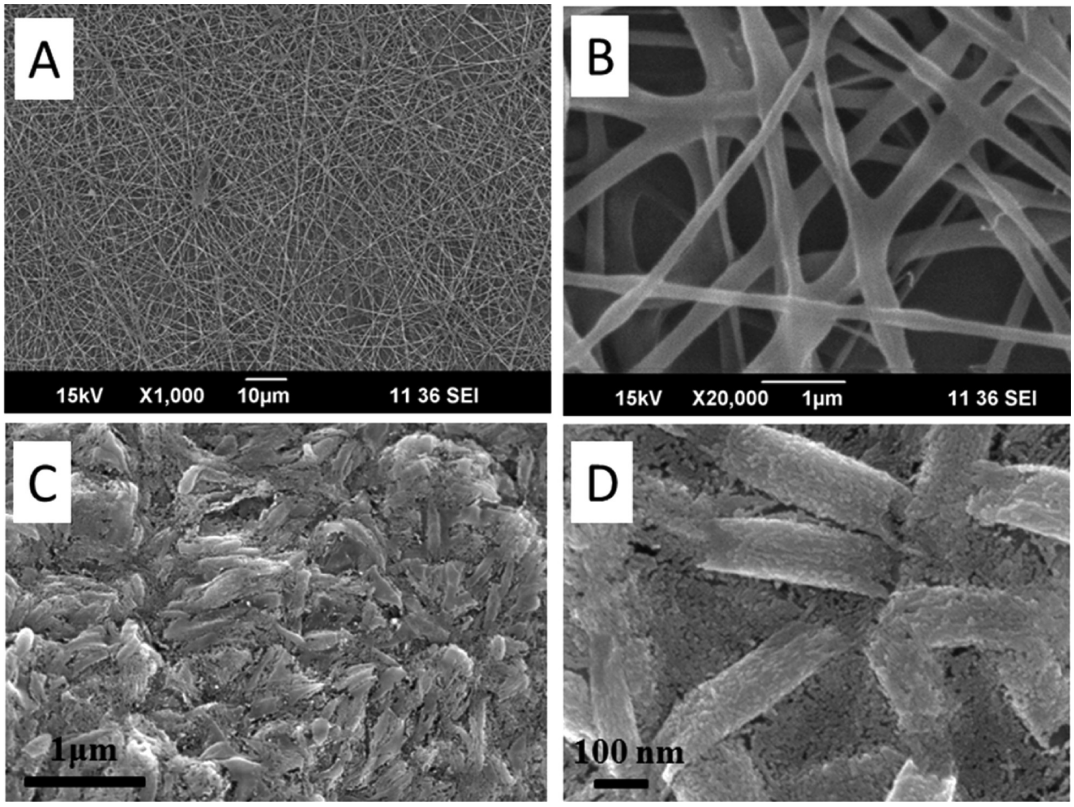

Figure 1. SEM images of the as-spun TiO_2−SiO_2−PVAc composite fibers at low and high resolutions (A and B, respectively). C and D show SEM images of the rice-shaped TiO_2−SiO_2 composite obtained after sintering.

in the literature especially when considering the efficiency from electrospun TiO_2-based materials.

EXPERIMENTAL SECTION

Materials and Methods. PVAc (poly(vinyl acetate), Mw = 500,000, Sigma-Aldrich, U.S.A.), methanol (absolute, Fischer scientific, Leicestershire, U.K.), acetic acid (LR, Nice Chemicals, India), titanium(IV) isopropoxide (TIP, 97%, Aldrich, Germany), tetraethoxysilane (TES, 98% GC grade, Alfa Aesar, U.K.), sodium hydroxide pellets (A.R grade, Nice Chemicals, India), hydrochloric acid (ACS, ISO Reag. Ph Eur, Merk KGaA, Germany), N719 dye (Dyesol, Australia), dibutyltin diacetate (DBTDA, Sigma-Aldrich, Germany), and ammonium fluoride (NH_4F, Aldrich, Germany) were used as received. The fluorine-doped tin oxide plates (FTO, sheet resistance of 8−10 Ω/□) were fabricated in-house by spray pyrolysis deposition (SPD) of FTO precursors, DBTDA, and NH_4F on Corning glass).

Fabrication of TiO_2−SiO_2 Composites. Rice-shaped TiO_2−SiO_2 composites were fabricated by an electrospinning process as per a previously reported methodology.[12] Briefly, 1.2 g of PVAc was dissolved in 10 mL of *N*,*N*-dimethylacetamide (DMAc) under sonication. Two milliliters of glacial CH_3COOH, 1.75 mL of TIP, and 0.25 mL of TES (i.e., TiO_2 to SiO_2 ratio of 7.2) were subsequently added to the polymer solution under sonication and stirred overnight to have a clear homogeneous solution. The solution was electrospun under the conditions of a flow rate of 1 mL/h, humidity level of ∼50%, and applied potential of 29 kV using a humidity-controlled electrospinning setup (IME Technologies, The Netherlands). The as-spun TiO_2−SiO_2−PVAc composite fibers were subsequently annealed at 450 °C for 3 h for crystallization of the metal oxide and degradation of the polymer. The rice-shaped TiO_2−SiO_2 composite was characterized by spectroscopy, microscopy, powder XRD, and BET surface area measurements.

Flower-like TiO_2 from Rice-Shaped TiO_2−SiO_2 Composite. The rice-shaped TiO_2−SiO_2 composite was treated with 5 M NaOH solution in a Teflon-lined steel autoclave at 180 °C for 24 h. A fluffy white precipitate of sodium titanate ($Na_2Ti_3O_7$) was obtained during the treatment, and the material was characterized using the techniques mentioned above. The $Na_2Ti_3O_7$ was washed several times with deionized water and then treated with 0.1 M HCl for exchange of Na^+ with H^+, and the resulting $H_2Ti_3O_7$ was converted into TiO_2 through a simple low-temperature annealing process (180 °C for 30 min). The flower-shaped TiO_2 obtained by the route was characterized by spectroscopy, microscopy, XRD, and BET surface area measurements and used for fabricating DSCs.

Fabrication of Fluorine-Doped Tin Oxide (FTO) Plates. The FTO plates were fabricated in-house by spray pyrolysis deposition of fluorine and tin oxide precursors on Corning glass. A mixture of 0.2 M DBTDA (in 2-propanol) and 9 M NH_4F (in water) was used for obtaining the precursors of the FTO coating. The mixture was spray-deposited on preheated (450 °C) Corning glass substrates by a professional spray-pyrolysis deposition (SPD) machine (SPD, Inc., Japan) and by controlling the number of spraying cycles; an optimum thickness of 800 nm for the FTO was deposited on the glass substrate. The sheet resistance of the FTO plates was ∼8−10 Ω/□).

Fabrication of Dye-Sensitized Solar Cells (DSCs). About 100 mg of the flower-shaped TiO_2 was mixed with 100 μL of polyester and made into a paste using ultrasonication (Misonix ultrasonic cleaner, 100W, 42 kHz). The paste was subsequently screen-printed on clean FTO plates (FTO plates were prewashed with soap solution, deionized water, methanol and 2-propanol and dried at 80 °C for 30 min) on an area of 0.20 cm^2 (square-shaped) and sintered at 450 °C for 3 h for removal of polyester, producing a porous TiO_2 film. The TiO_2 films were subsequently dipped in 0.5 mM N719 dye solution for 24 h for saturate chemisorption of the dye and washed with acetonitrile for removal of the physisorbed dyes. The cell was coupled against a Pt/FTO counter electrode in the presence of a spacer. Electrolyte was filled-in using the vacuum backfilling process (electrolyte filling machine, SPD Laboratory, Inc.). DSCs were characterized by current−voltage (*I*-*V*), incident photon-to-current conversion efficiency (IPCE), and electrochemical impedance spectroscopy (EIS).

dx.doi.org/10.1021/sc500642c | ACS Sustainable Chem. Eng. 2014, 2, 2772−2780

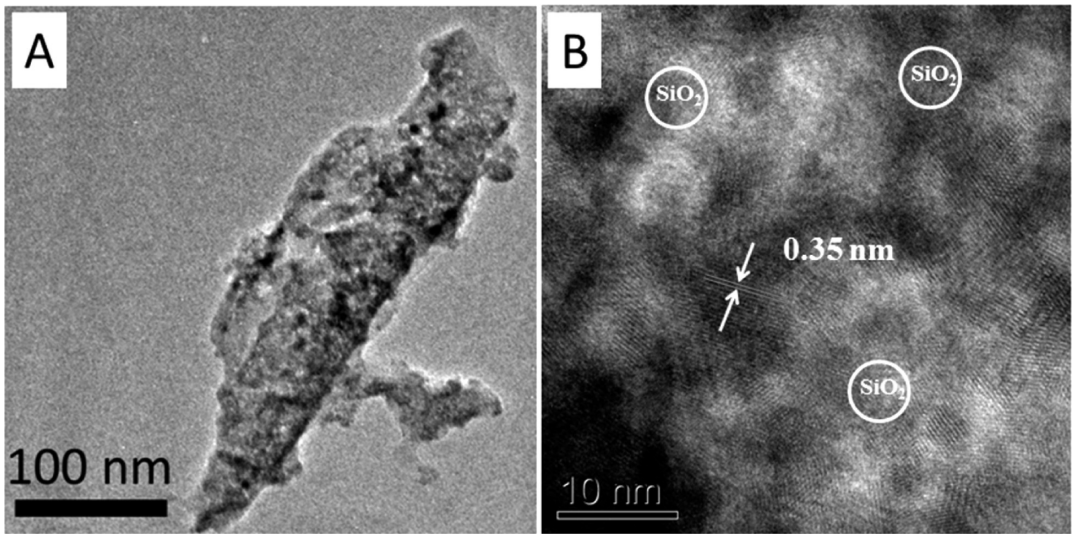

Figure 2. (A) TEM image of a rice-shaped TiO_2−SiO_2 composite. (B) Lattice-resolved TEM image showing the 0.35 nm lattice spacing. Amorphous regions marked with white circles could be the SiO_2 locations in the composite.

Characterization Techniques and Details. Scanning electron microscopy (SEM) was performed using a JSM 6490 LA (JEOL-Tokyo, Japan) microscope (operating voltage at 15 kV). A thin film of gold was sputtered on the materials using a sputter-coating machine (JEOL-Tokyo, Japan) before the SEM measurements. Absorption spectra of the TiO_2 films (in diffuse-reflectance spectrum, DRS, mode) were measured by a Varian Cary 5000 spectrometer. Transmission electron microscopy (TEM) was performed using a Tecnai G2 TF20 S-TWIN machine at an operating voltage of 200 kV. The materials were suspended in methanol under mild sonication, and a drop of the solution was cast on a carbon-coated copper grid and dried under ambience and vacuum before TEM measurements. Brunauer−Emmett−Teller (BET) surface area, pore size distribution, and average pore volume were measured using a Tristar II 3020 surface area analyzer (Micromeritics, U.S.A.) under standard measurement conditions. The powder XRD was performed using an X'pert pro PAN analytical instrument (data interval of 0.03°) operated at a current of 30 mA with a voltage of 40 kV. X-ray photoelectron spectroscopy (XPS, Kratos Analytical, U.K.) and Raman spectroscopy (Witec confocal Raman-300 AR instrument using an excitation laser of 488 nm and power of 0.6 μW; spot size was >2 μm) were carried out as per standard procedures. $I-V$ characteristics of the solar cells were obtained by a solar simulator under AM1.5G condition (Newport Oriel class A-Solar simulator, U.S.A.). The incident photon-to-current conversion efficiency (IPCE) was measured using an Oriel Newport (QE−PV-SI/QE) IPCE Measurement kit (U.S.A.).

RESULTS AND DISCUSSION

Figure 1A and B show low- and high-magnification SEM images of the as-spun TiO_2−SiO_2−PVAc composite fibers. The fibers were continuous with an average fiber diameter of ∼200 nm (estimated using ImageJ software). The fibers upon sintering at 450 °C resulted in the formation of a rice-shaped TiO_2−SiO_2 composite (Figure 1C and D). Figure 1C and D, respectively, show a low- and high-resolution SEM image of the rice-shaped composite. Figure 1D implies that each rice-like structure has an average diameter of 150 nm and is made of small spherical particles of ∼5−10 nm sizes.

Figure 2A shows a TEM image of a rice-like structure. A lattice-resolved image is shown in Figure 2B, and the lattice spacing was found to be 0.35 nm, which corresponds to the anatase phase of TiO_2 in the TiO_2−SiO_2 composite. There was no lattice spacing corresponding to the SiO_2 in the composite implying its amorphous nature (areas marked with white circles in Figure 2B could be the SiO_2 regions). The amorphous nature of SiO_2 in the composite was further confirmed by powder XRD spectrum (Figure 3), which shows peaks corresponding to the anatase TiO_2 alone. The peaks are indexed in the spectrum itself.

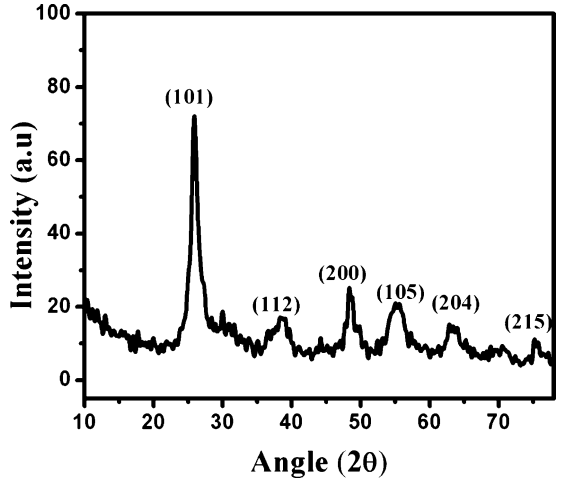

Figure 3. Powder XRD spectrum of rice-like TiO_2−SiO_2 composite. TiO_2 peaks are indexed in the spectrum itself (JCPDS file no. 21-1272).

The elemental composition and oxidation state of the elements in the sample were analyzed using XPS. The survey spectrum of the TiO_2−SiO_2 composite (Figure 4A) shows its elemental composition, which is marked in the spectrum. Figure 4B, C, and D show the high-resolution spectrum of Ti, O, and Si, respectively. For Ti, the $2p_{1/2}$ and $2p_{3/2}$ peaks were centered at 464.77 and 459.16 eV (Figure 4B), respectively, that corresponds to a spin−orbit coupling of 5.6 eV. The binding energy (BE) of oxygen (at 530.3 eV) can be deconvoluted to three peaks centered at 529.69, 530.71, 531.72 eV, respectively, corresponding Ti−O−Ti, Si−O−Si, and Si−O−Ti bonds.[22] This confirms that SiO_2 is embedded into the TiO_2 lattice through a Si−O−Ti chemical bond.[24] The BE of silicon was located at 102.85 eV corresponding to the Si^{4+} oxidation state.[22]

Figure 5A shows the SEM image of the sheet-like $Na_2Ti_3O_7$ obtained by the titanate process.[25−27] Each sheet-like structure

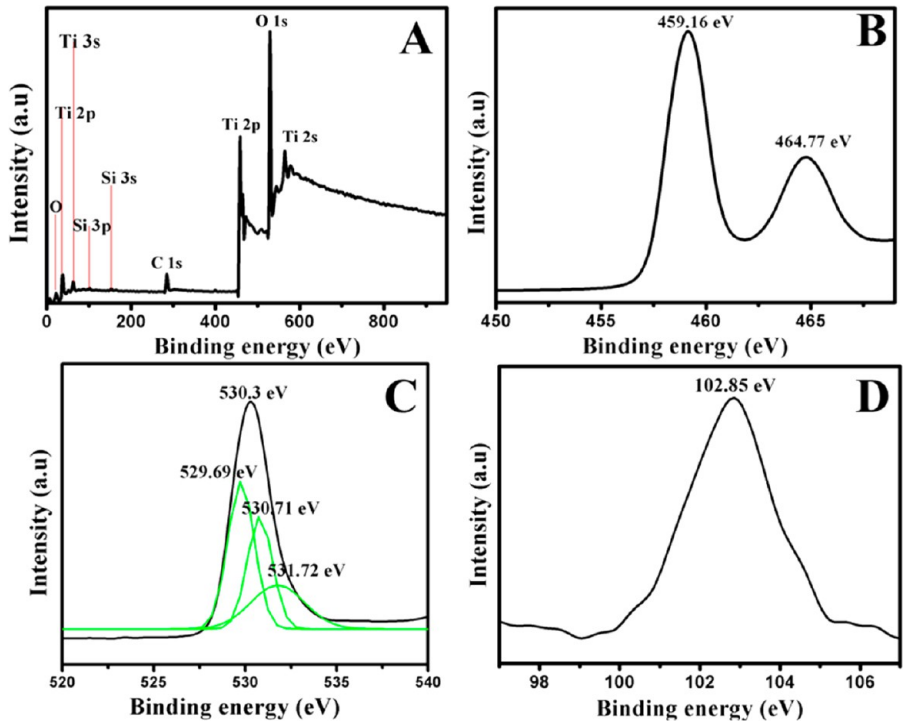

Figure 4. (A) Wide XPS spectrum of TiO_2−SiO_2 composite and high-resolution spectrum of (B) Ti, (C) O, and (D) Si, respectively.

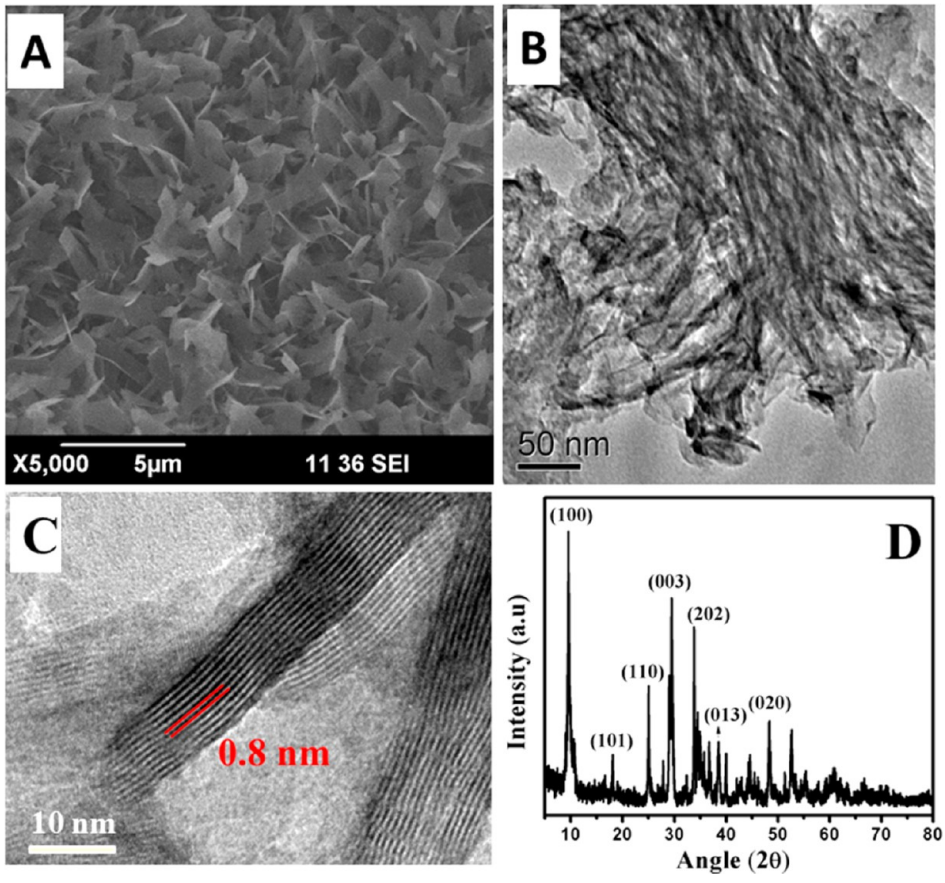

Figure 5. (A) SEM image of the sodium titanate sheets. (B) TEM image of a sheet showing its layered nature. (C) High-resolution TEM of the sodium titanate sheet showing the layer spacing. (D) XRD spectrum of sodium titanate (JCPDS file no. 72-0148).

was about 1−2 μm in length and ∼100 nm in thickness. Figure 5B shows the TEM image revealing its layered nature. The spacing between the layers was found to be 0.8 nm from high-resolution TEM as shown in Figure 5C. The XRD spectrum of

dx.doi.org/10.1021/sc500642c | ACS Sustainable Chem. Eng. 2014, 2, 2772−2780

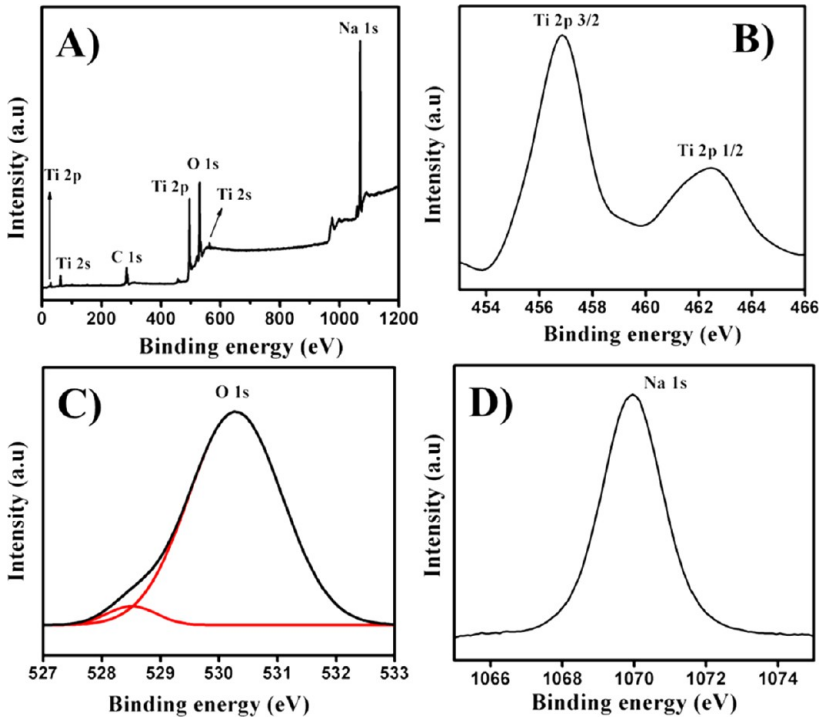

Figure 6. (A) Wide XPS spectrum of sodium titanate and high-resolution spectrum of (B) Ti 2p, (C) O 1s, and (D) Na 1s regions.

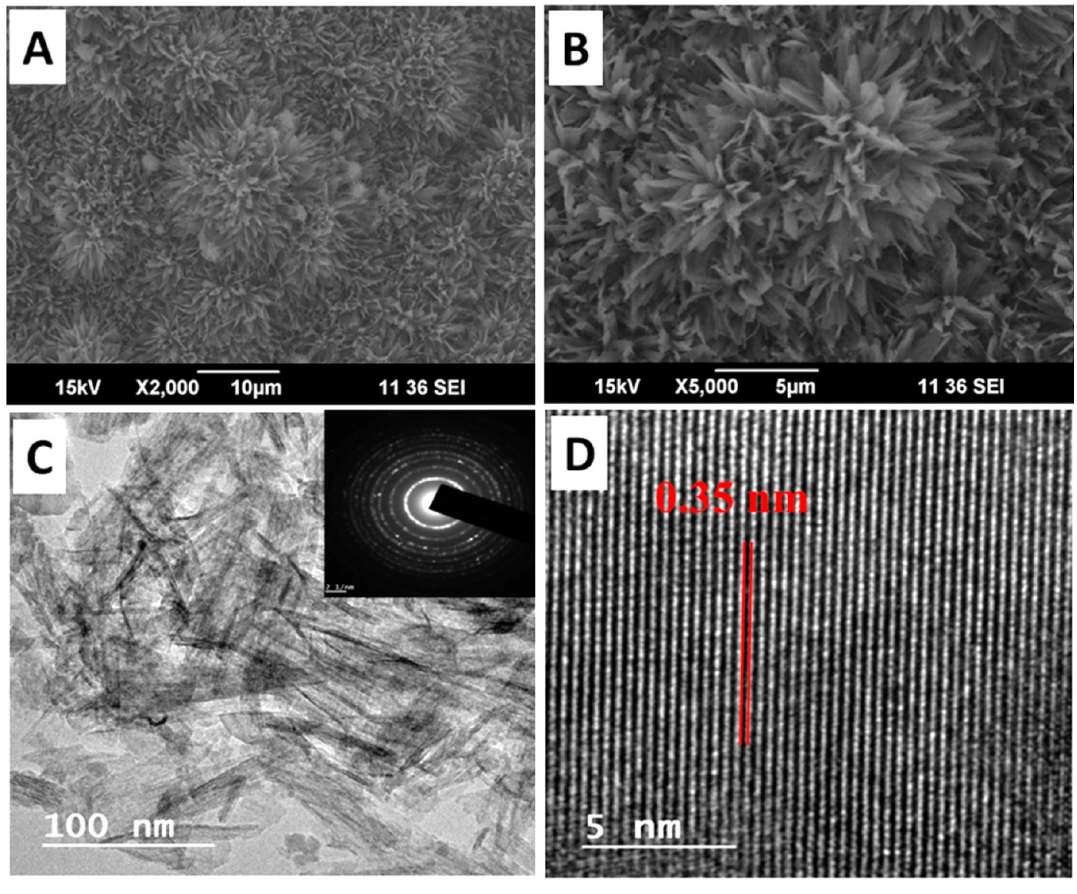

Figure 7. (A) Low magnification SEM image of TiO_2 3-D mesoflowers. (B) High-resolution SEM image of the mesoflowers. (C) TEM image of a part of the mesoflower petal showing that the mesoflowers consist of nanosheets (inset, SAED pattern showing polycrystainility). (D) High-resolution TEM image showing the 0.35 nm lattice spacing of the sample.

dx.doi.org/10.1021/sc500642c | *ACS Sustainable Chem. Eng.* 2014, 2, 2772−2780

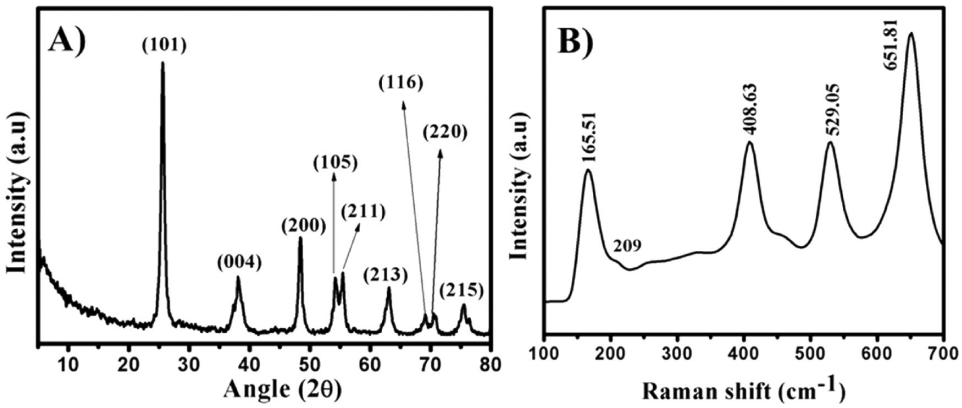

Figure 8. (A) Powder XRD pattern confirming the highly crystalline and anatase nature of TiO_2 3-D mesoflowers (JCPDS file no. 21−1272). (B) Raman spectrum of TiO_2 mesoflowers.

the $Na_2Ti_3O_7$ is given in Figure 5D. The XRD peak at $2\theta \sim 10°$ is characteristic of $Na_2Ti_3O_7$ and its layered nature.[28] The elemental composition of titanate and the oxidation state of the elements were further assessed by XPS (Figure 6) in which Figure 6A shows the wide spectrum and Figure 6B and C shows the high-resolution spectra of Ti (at 456.86 and 462.45 eV) and O (at 530.28 eV), respectively. The peak, corresponding to oxygen, can be deconvoluted into two peaks, i.e., at 528.45 and 530.28 eV corresponding to Ti−O−Na and Ti−O−Ti bonds, respectively.

The complete removal of SiO_2 is evident from the absence of peaks corresponding to Si−O−Si and Si−O−Ti bonds. The peak observed at 1069.95 eV corresponds to Na 1s (Figure 6D), which confirms the presence of sodium in the lattice of the sample. The $Na_2Ti_3O_7$ upon acidification (formation of $H_2Ti_3O_7$ by the hydrolysis of $Na_2Ti_3O_7$) and low-temperature sintering (180 °C) resulted in the formation of TiO_2 mesoflowers through self-assembly of the sheet-like structures.[17]

Figure 7A and B shows a large area and resolved SEM images of the TiO_2 3-D mesoflowers. The TEM image (Figure 7C) of a part of the leaf-like feature showed that the petals of the leaf are made of nanosheets. The lattice spacing obtained from HRTEM (Figure 7D) was 0.35 nm, which coincides with the characteristic (101) spacing of anatase TiO_2. The high crystallinity of the TiO_2 was evident from the SAED pattern shown in the inset of Figure 7C.

The XRD spectrum (Figure 8A) reveals that the 3-D mesoflower TiO_2 is highly crystalline in nature (peaks are indexed in the spectrum itself) with the maximum intensity peak centered at $2\theta = 25°$, which corresponds to the (101) plane of anatase TiO_2. It is to be noted that the anatase phase is preferred over other forms of TiO_2 for DSCs because of the concentration of hydroxyl density along the (101) plane.[29] In the Raman spectrum of anatase TiO_2 (Figure 8B), the peaks at 408.63 and 529.05 cm^{-1} represent B_g1 and A_g1 vibrational modes, respectively. The E_g vibrational modes of TiO_2 appear at 165.51, 209, and 651.81 cm^{-1}.[30]

XPS was also performed to confirm the elemental composition and oxidation state of 3-D mesoflower TiO_2. The wide spectrum is shown in Figure 9A. In the case of Ti 2p (Figure 9B), splitting of peaks was observed due to spin−orbit coupling. The binding energies of Ti $2p_{3/2}$ and Ti $2p_{1/2}$ were centered at 460.88 and 466.77 eV, respectively. The spin−orbit coupling value for Ti 2p is about 5.89 eV. The single nondeconvolutable peak at 531.7 eV (Figure 9C) corresponding to oxygen confirms the absence of

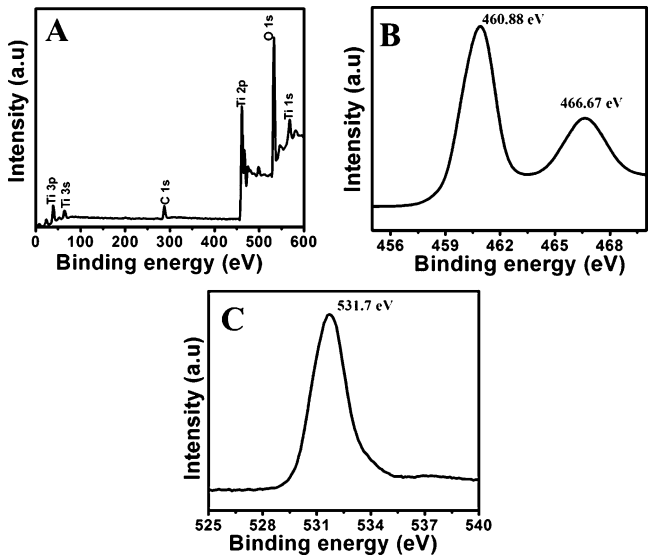

Figure 9. (A) XPS wide spectrum of the TiO_2 3-D mesoflowers and high-resolution spectrum of (B) titanium and (C) oxygen.

impurity. The shift toward higher BE observed in pure TiO_2 compared to the TiO_2−SiO_2 composite further confirms that only the Ti−O−Ti bond is present in the sample. The BET surface area analysis was used to obtain surface area, average pore diameter, and pore volume. The N_2 sorption isotherm and BJH pore size distribution are shown in Figure 10A and B, respectively. The BET surface area for 3-D mesoflowers was about 166 m^2/g with average pore diameter of 6.55 nm and pore volume of 0.27 cm^2/g, while P-25 has a surface area about 40 m^2/g.

Photovoltaic Performance of DSCs. The photovoltaic performance of 3-D mesoflower TiO_2 was compared against P-25. The film thickness of TiO_2 was optimized as 14 μm for 3-D mesoflowers (Table 1).

The best efficiency for mesoflower TiO_2 was about 8.32% compared to P-25 (6.37%) (Figure 11A). The open-circuit voltage for the mesoflower TiO_2 DSCs was higher (764 mV) compared P25 TiO_2 (i.e., 732 mV). The fill factor for DSC fabricated using mesoflowers (73%) was found to be higher than P-25 (70%). A remarkable improvement in current density was noticed for mesoflower TiO_2 (14.84 mA cm^{-2}) in comparison to P-25 (12.39 mA cm^{-2}). The IPCE measurement gives photocurrent response of the cell as a function of the wavelength.

dx.doi.org/10.1021/sc500642c | ACS Sustainable Chem. Eng. 2014, 2, 2772−2780

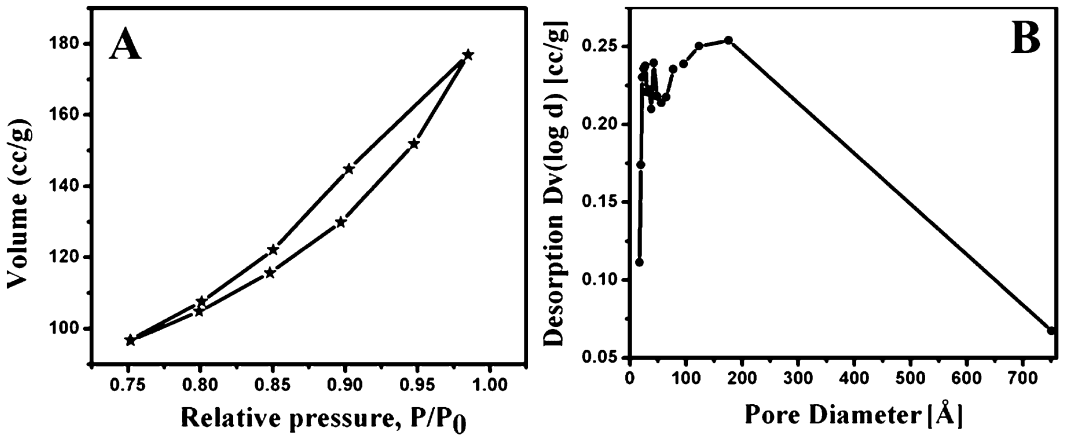

Figure 10. (A) N_2-adsorption isotherms and (B) Barrett–Joyner–Halenda (BJH) pore-size distribution curves of TiO_2 3-D mesoflowers.

Table 1. Variation of Photovoltaic Parameters of DSCs with Respect to Thickness of TiO_2 Film

thickness of the film (μm)	open-circuit voltage (V)	current density (mA cm^{-2})	fill factor (%)	efficiency (%)
10	0.738	11.65	72.67	6.26
12	0.757	14.72	73.02	8.14
14	0.764	14.84	73.36	8.32
16	0.753	14.03	72.01	7.62

The IPCE peak observed was about 80% for the mesoflower TiO_2 at 530 nm (corresponding to the absorption maximum of the dye), whereas that is only 66% for the P-25 (Figure 11B).

The commendable enhancement in the efficiency of the 3-D mesoflower DSC was because of the enhancements in current density, open-circuit voltage, and fill factor in comparison to that of P-25. We have analyzed these factors separately. The photocurrent enhancement was investigated based on the following. Generally, the high internal surface area and light scattering of TiO_2 contribute to the improvement of photocurrent in DSCs. The high internal surface area of mesoflower TiO_2 facilitates more chemisorption of dye molecules on the TiO_2 film. The photocurrent generation in DSCs depends on the dye loading on the porous TiO_2 film. To quantify the dye loading on the photoelectrode film, we have deloaded dye from an electrode using a 0.1 M NaOH solution and quantified that using a UV–vis spectrometer. The absorbance spectrum reveals that the 3-D mesoflowers have higher dye loading compared to P-25 (Figure 12A). Thus, the higher dye loading in the electrode made of mesoflowers contributed partly to the increased photocurrent.

The building blocks of TiO_2 mesoflowers are nanosheets with dimensions of about 2–3 μm. The TiO_2 mesoflowers with dimensions comparable to the wavelength of incident photons scatter light effectively within the photoanode (Mie scattering), which would increase the interaction of light with dye molecules.[31] The light scattering of both P-25 and the mesoflowers is compared in Figure 12B. The diffused reflectance by the TiO_2 mesostructures is superior especially in the red part of the spectrum compared to that of P-25. Thus, the light confinement within the photoanode due to enhanced light scattering also contributed to the enhanced photocurrent.

Electrochemical impedance spectroscopy (EIS) was performed to obtain recombination resistance (Rct)[32−34] of the DSCs fabricated using TiO_2 mesoflowers. EIS was performed under dark with an applied forward voltage of 0.70 V. In the Nyquist plot (one of the common forms of the EIS result), generally three semicircles are obtained, in which each one indicates charge transfer at different interfaces of a DSC. The three semicircles and their corresponding charge transfer processes are as follows: charge transfer at the counter electrode/electrolyte (higher frequency range), charge transfer at the oxide/electrolyte interface (Rct) (medium frequency range), and ion diffusion in the electrolyte (lower frequency range).[35] Because we are interested in obtaining a charge transport property at the TiO_2–dye–electrolyte interface, we have obtained R_{ct} from the semicircle at medium frequency range (corresponds to resistance against recombination of electron

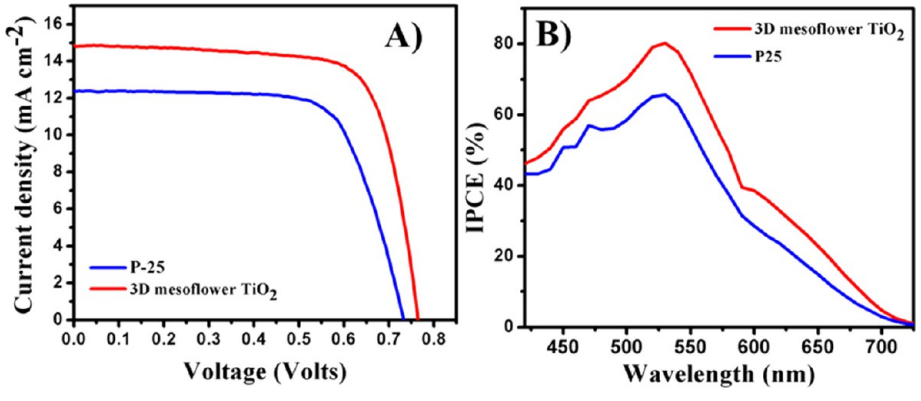

Figure 11. (A) *J-V* graph and (B) IPCE spectrum comparing the 3-D mesoflower and P-25 TiO_2.

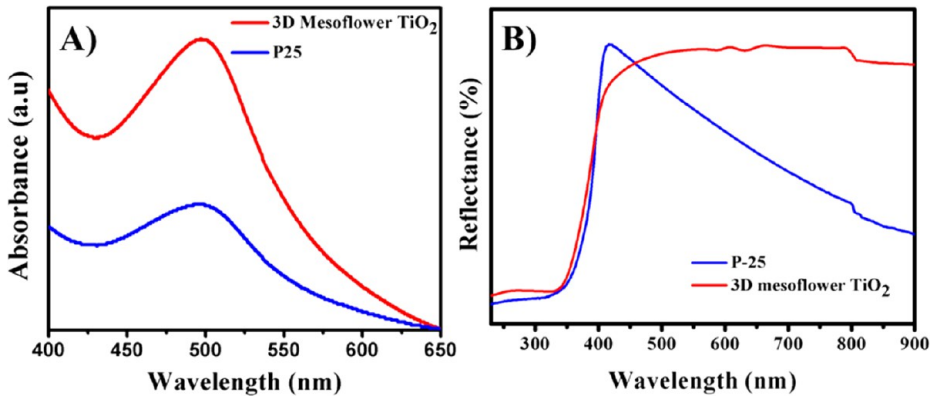

Figure 12. (A) Absorbance spectrum of the dye solution, deloaded from photoelectrodes in NaOH. (B) Reflectance spectrum showing enhanced light scattering in the red part the spectrum for the 3-D mesoflower.

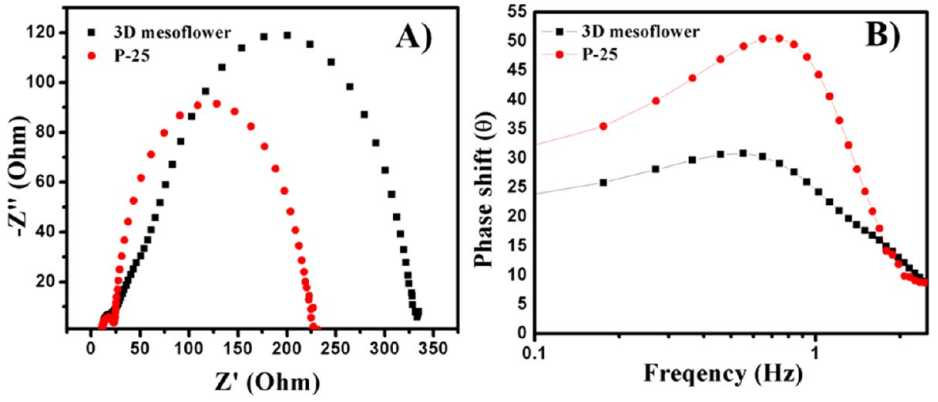

Figure 13. (A) Nyquist plot showing higher recombination resistance offered by 3-D mesoflower TiO_2 compared to P-25 in DSCs. (B) Bode plot showing increased lifetime for the 3-D mesoflower TiO_2 DSC.

from semiconductor oxide network to I_3^- of electrolyte) of both P-25 and mesoflower TiO_2 in Figure 13A. The higher recombination resistance (parallel resistance in equivalent circuit of the solar cell) would facilitate electron flow through the external load with a lesser recombination of electrons to the electrolyte. This is further reflected in the lifetime of the electron in the semiconductor oxide network. The peak in the bode plot (Figure 13B) corresponding to the second semicircle (at medium frequency) shifted to lower frequency (3.58 Hz) for the 3-D mesoflower compared to P-25 (5.48 Hz). The corresponding lifetimes for the 3-D mesoflower and P-25 were calculated as 44.3 and 29 ms, respectively. The lesser electron recombination in the 3-D mesoflower is reflected in the form of enhanced V_{oc} and current density in the DSC. It must also be mentioned that while reduced recombinations partly explain the reasons for the observed high V_{oc} for the mesoflower DSC, this can also be partly attributed to the difference in the band-edge positions of the materials because V_{oc} is the difference between the Fermi level of TiO_2 and the redox potential of the electrolyte. Mesoflower TiO_2 is ~100% anatase, while P-25 is a mixture of ~75% anatase and ~25% rutile forms. The conduction band edge of anatase TiO_2 is 0.2 eV above (more negative) compared to that of rutile. In the case of P-25, the apparent Fermi level tends to shift to lower values than the mesoflowers because it is a mixture of rutile and anatase.[36−38] We can thus conclude that the high efficiency of the 3-D mesoflowers is because of the increased J_{sc}, V_{oc}, and FF in comparison to commercial P-25.

CONCLUSIONS

We have synthesized three-dimensional flower-like TiO_2 mesostructures with desirable properties such as high internal surface area, high light scattering ability, and enhanced electron mobility for DSC application. Here, electrospun TiO_2−SiO_2 rice-like nanostructures hydrothermally treated in concentrated NaOH, followed by washing and chemical treatment in diluted HCl, and later by low-temperature sintering produces anatase TiO_2 3-D mesoflowers. The photovoltaic performance of the highly crystalline material obtained through a titanate route with high surface area (166 m^2/g) was investigated (8.3%) and found superior to commercially available TiO_2 (6.37%, P-25, Degussa). Further, scientific reasons for superior photovoltaic performance were probed through well-established characterization techniques in the dye-sensitized solar research area.

AUTHOR INFORMATION

Corresponding Author

*E-mail: sreekumarannair@aims.amrita.edu.

Notes

The authors declare no competing financial interest.

ACKNOWLEDGMENTS

The authors thank the Ministry of New and Renewable Energy (MNRE), Government of India for financial assistance.

REFERENCES

(1) Grätzel, M. Photoelectrochemical cells. *Nature* **2001**, *414*, 338−344.
(2) Hagfeldt, A.; Grätzel, M. Light-induced redox reactions in nanocrystalline systems. *Chem. Rev.* **1995**, *95*, 49−68.
(3) Linsebigler, A. L.; Lu, G.; Yates, J. T. Photocatalysis on TiO_2 surfaces: Principles, mechanisms and selected results. *Chem. Rev.* **1995**, *95*, 735−758.
(4) Millis, A.; Le Hunte, S. An overview of semiconductor photocatalysis. *J. Photochem. Photobiol., A* **1997**, *108*, 1−35.
(5) Zhu, P.; Wu, Y.; Reddy, M. V.; Nair, A. S.; Chowdari, B. V. R.; Ramakrishna, S. Long term cycling studies of electrospun TiO_2 nanostructures and their composites with MWCNTs for rechargeable Li-ion batteries. *RSC Adv.* **2012**, *2*, 531−537.
(6) Ganesh, V. A.; Raut, H. K.; Nair, A. S.; Ramakrishna, S. A review on self-cleaning coatings. *J. Mater. Chem.* **2011**, *21*, 16304−16322.
(7) Ganesh, A. A.; Dinachali, S. S.; Nair, A. S.; Ramakrishna, S. Robust superamphiphobic film from electrospun TiO_2 nanostructures. *ACS Appl. Mater. Interfaces* **2013**, *5*, 1527−1532.
(8) Reddy, M. V.; Subba Rao, G. V.; Chowdari, B. V. R. Metal oxides and oxysalts as anode materials for Li ion batteries. *Chem. Rev.* **2013**, *113*, 5364−5457.
(9) Zhu, P.; Wu, Y.; Reddy, M. V.; Nair, A. S.; Chowdari, B. V. R.; Ramakrishna, S. Long term cycling studies of electrospun TiO_2 nanostructures and their composites with MWCNTs for rechargeable Li-ion batteries. *RSC Adv.* **2012**, *2*, 531−537.
(10) O'Regan, B.; Grätzel, M. A Low-cost, high-efficiency solar cell based on dye-sensitized colloidal TiO_2 films. *Nature* **1991**, *353*, 737−740.
(11) Nair, A. S.; Peining, Z.; Babu, V. J.; Shengyuan, Y.; Ramakrishna, S. Anisotropic TiO_2 nanomaterials in dye-sensitized solar cells. *Phys. Chem. Chem. Phys.* **2011**, *13*, 21248−21261.
(12) Nair, A. S.; Shengyuan, Y.; Peining, Z.; Ramakrishna, S. Rice grain-shaped TiO_2 mesostructures by electrospinning for dye-sensitized solar cells. *Chem. Commun.* **2010**, *46*, 7421−7423.
(13) Nair, A. S.; Jose, R.; Shengyuan, Y.; Ramakrishna, S. A simple recipe for an efficient TiO_2 nanofiber-based dye-sensitized solar cell. *J. Colloid Interface Sci.* **2011**, *353*, 39−45.
(14) Song, M. Y.; Kim, D. K.; Ihn, K. J.; Jo, S. M.; Kim, D. Y. Electrospun TiO_2 electrodes for dye-sensitized solar cells. *Nanotechnology* **2004**, *15*, 1861.
(15) Kokubo, H.; Ding, B.; Naka, T.; Tsuchihira, H.; Shiratori, S. Multicore cable-like TiO_2 nanofibrous membranes for dye-sensitized solar cells. *Nanotechnology* **2007**, *18*, 165604.
(16) Peining, Z.; Yongzhi, W.; Reddy, M. V.; Nair, A. S.; Shengjie, P.; Sharma, P.; Peterson, V. K.; Chowdari, B.V. R.; Ramakrishna, S. TiO_2 nanoparticles synthesized by the molten salt method as a dual functional material for dye-sensitized solar cells. *RSC Adv.* **2012**, *2*, 5123−5126.
(17) Arun, T. A.; Chacko, D. K.; Madhavan, A. A.; Deepak, T. G.; Anjusree, G. S.; Sara, T.; Ramakrishna, S.; Nair, S. V.; Nair, A. S. Flower-shaped anatase TiO_2 mesostructures with excellent photocatalytic properties. *RSC Adv.* **2014**, *4*, 1421−1424.
(18) Deepak, T. G.; Anjusree, G. S.; Narendra Pai, K. R.; Devika, S.; Nair, S. V.; Nair, A. S. Cabbage leaf-shaped two-dimensional TiO_2 mesostructures for efficient dye-sensitized solar cells. *RSC Adv.* **2014**, *4*, 27084−27090.
(19) Nair, A. S.; Zhu, P.; Babu, V. J.; Yang, S.; Krishnamoorthy, T.; Murugan, R.; Peng, S.; Ramakrishna, S. TiO_2 derived by titanate route from electrospun nanostructures for high-performance dye-sensitized solar cells. *Langmuir.* **2012**, *28*, 6202−6206.
(20) Kasuga, T.; Hiramatsu, M.; Hoson, A.; Sekino, T.; Niihara, K. Titania nanotubes prepared by chemical processing. *Adv. Mater.* **1999**, *11*, 1307−1311.
(21) Kasuga, T.; Hiramatsu, M.; Hoson, A.; Sekino, T.; Niihara, K. Formation of titanium oxide nanotube. *Langmuir* **1998**, *14*, 3160−3163.
(22) Su, C.; Lin, K.-F.; Lin, Y.-H.; You, B.-H. Preparation and characterization of high-surface-area titanium dioxide by sol-gel process. *J. Porous. Mater.* **2006**, *13*, 251−258.
(23) Tsai, C. C.; Teng, H. Structural features of nanotubes synthesized from NaOH treatment on TiO_2 with different post-treatments. *Chem. Mater.* **2006**, *18*, 367−373.
(24) Zhang, H.; Luo, X.; Xu, J.; Xiang, B.; Yu, D. Synthesis of TiO_2/SiO_2 core/shell nanocable arrays. *J. Phys. Chem. B* **2004**, *108*, 14866−14869.
(25) Kiatkittipong, K.; Ye, C.; Scott, J.; Amal, R. Understanding hydrothermal titanate nanoribbon formation. *Cryst. Growth Des.* **2010**, *10*, 3618−3625.
(26) Zhou, W.; Gai, L.; Hu, P.; Cui, J.; Liu, X.; Wang, D.; Li, G. Phase transformation of TiO_2 nanobelts and TiO_2(B)/anatase interface. *Cryst. Eng. Comm* **2011**, *13*, 6643−6649.
(27) Huang, J.; Cao, Y.; Wang, M.; Huang, C.; Deng, Z.; Tong, H.; Liu, Z. Tailoring of low-dimensional titanate nanostructures. *J. Phys. Chem. C* **2010**, *114*, 14748−14754.
(28) Morgado, E., Jr.; de Abreu, M. A. S.; Moure, G. T.; Marinkovic, B. A.; Jardim, P. M.; Araujo, A. S. Characterization of nanostructured titanates obtained by alkali treatment of TiO_2-anatases with distinct crystal sizes. *Chem. Mater.* **2007**, *19*, 665−676.
(29) Zuleta, M.; Edvinsson, T.; Yu, S.; Ahmadi, S.; Boschloo, G.; Göthelid, M.; Hagfeldt, A. Light-induced rearrangements of chem-isorbed dyes on anatase (101). *Phys. Chem. Chem. Phys.* **2012**, *14*, 10780−10788.
(30) Choi, H. C.; Jung, Y. M.; Kim, B. N. Size effects in the raman spectra of TiO_2 nanoparticles. *Vib. Spectrosc.* **2005**, *37*, 33−38.
(31) Zhang, Q.; Myers, D.; Lan, J.; Jenekhebc, S. A.; Cao, G. Applications of light scattering in dye-sensitized solar cells. *Phys. Chem. Chem. Phys.* **2012**, *14*, 14982−14998.
(32) Bisquert, J. Theory of the impedance of electron diffusion and recombination in a thin layer. *J. Phys. Chem. B* **2002**, *106*, 325−333.
(33) Kern, R.; Sastrawan, R.; Ferber, J.; Stangl, R.; Luther, J. Modeling and interpretation of electrical impedance spectra of dye solar cells operated under open-circuit conditions. *Electrochim. Acta* **2002**, *47*, 4213−4277.
(34) Bisquert, J.; Vikhrenko, V. S. Interpretation of the time constants measured by kinetic techniques in nanostructured semiconductor electrodes and dye-sensitized solar cells. *J. Phys. Chem. B* **2004**, *108*, 2313−2322.
(35) Park, K.; Zhang, Q.; Myers, D.; Cao, G. Charge transport properties in TiO_2 network with different particle sizes for dye sensitized solar cells. *ACS Appl. Mater. Interfaces.* **2013**, 1044−1052.
(36) Kavan, L.; Gratzel, M.; Gilbert, S. E.; Klemenz, C.; Scheel, H. J. Electrochemical and photoelectrochemical investigation of single-crystal anatase. *J. Am. Chem. Soc.* **1996**, *118*, 6716−6723.
(37) Xiong, G.; Shao, R.; Droubay, T. C.; Joly, A. G.; Beck, K. M.; Chambers, S. A.; Hess, W. P. Photoemission electron microscopy of TiO_2 anatase films embedded with rutile nanocrystals. *Adv. Funct. Mater.* **2007**, *17*, 2133−2138.
(38) Scanlon, D. O.; Dunnill, C. W.; Buckeridge, J.; Shevlin, S. A.; Logsdail, A. J.; Woodley, S. M.; Catlow, C. R. A.; Powell, M. J.; Palgrave, R. J.; Parkin, I. P.; Watson, G. W.; Keal, T. W.; Sherwood, P.; Walsh, A.; Sokol, A. A. Band alignment of rutile and anatase TiO_2. *Nat. Mater.* **2013**, *12*, 798−801.